Materials Research Proceedings 57 (2025) 99-106 https://doi.org/10.21741/9781644903735-12

Effect of process parameters on $AlCoCr_2FeMo_{0.5}Ni$ high-entropy alloy coatings produced using laser directed energy deposition

Chiara GIANASSI[1,a *], Erica LIVERANI[1,b], Alessandro ASCARI[1,c] and Alessandro FORTUNATO[1,d]

[1]Department of Industrial Engineering (DIN), Viale del Risorgimento 2, Alma Mater Studiorum – University of Bologna, Bologna, Italy

[a]chiara.gianassi2@unibo.it, [b]erica.liverani2@unibo.it, [c]a.ascari@unibo.it, [d]alessandro.fortunato@unibo.it

Keywords: Additive Manufacturing, Direct Energy Deposition (DED), Laser Processes, High-Entropy Alloys, Coating, Aeronautical & Aerospace

Abstract. In the aerospace sector, High-Entropy Alloys (HEAs) are emerging as promising alternatives to nickel superalloys for turbine components due to their exceptional thermal stability, fatigue strength, and corrosion resistance. HEAs, composed of five or more elements in near-equal proportions, typically form stable crystal structures. Additive manufacturing, notably Laser Directed Energy Deposition (L-DED), addresses the limitations of conventional fabrication methods. In this study, L-DED was used to print the $AlCoCr_2FeMo_{0.5}Ni$ HEA to produce defect-free deposits with strong substrate adhesion. Single-track and multi-track tests assessed the impact of laser power, scanning speed, and powder feed rate on defects, with optimal conditions identified through optical microscopy. SEM analysis provided insights into the microstructure and composition, while 3D mapping characterized the surface morphology and roughness. The results demonstrate the potential of L-DED for advanced HEA manufacturing.

Introduction

The aerospace industry is at the forefront of engineering innovation, requiring components capable of withstanding extreme operating conditions such as elevated temperatures and intense mechanical stresses. Turbine engine design has continually evolved to enhance power, fuel efficiency, and safety, demanding higher compression ratios and turbine inlet temperatures. As a result, materials engineering plays a crucial role in the development of high-performance turbines. Nickel-based superalloys, renowned for their strength and creep resistance, are the current material of choice for turbine engines [1]. However, their high density (approximately 9 $g \cdot cm^{-3}$) and reliance on critical raw materials have spurred interest in alternative solutions, including the evaluation of innovative materials such as High Entropy Alloys (HEAs). HEAs are a class of materials distinguished by their unique composition, typically consisting of five or more principal elements in equiatomic or near-equiatomic proportions (5–35%). Their high configurational entropy, combined with sluggish diffusion, lattice distortion, and the cocktail effect, imparts them unique mechanical and physical properties, including exceptional tensile strength, hardness and thermal stability [2]. While conventional fabrication methods like casting and sintering are commonly used for HEAs, these approaches limit design flexibility and control over features such as porosity and microstructure. Additive manufacturing (AM) techniques, particularly Directed Energy Deposition (DED), allow to overcome these limitations, enabling greater control over process and shorter production cycles. Among HEAs, AlCoCrFeNi alloys have emerged as promising candidates for aerospace applications due to their high strength, hardness, and oxidation resistance. Previous studies have explored their microstructure, phase composition, and mechanical properties [3, 4]. Moreover, researchers have investigated the effects of varying alloying elements [5], discovering that aluminum content significantly influences the formation of

Materials Research Proceedings 57 (2025) 99-106 https://doi.org/10.21741/9781644903735-12

BCC structures [5] [6], and that the addition of molybdenum promotes the formation of high-hardness sigma-phase intermetallics [7]. Despite substantial progress, much of the existing research has focused on microstructural analysis and small-scale samples, with limited attention to the optimization of process parameters or large-scale depositions. This study aims to address these gaps by utilizing a pre-mixed $AlCoCr_2FeMo_{0.5}Ni$ alloy powder produced through gas atomization to ensure uniform chemical composition. Samples of progressively larger sizes were deposited using a single-track to multi-track approach in an effort to optimize the key process parameters, i.e. laser power, scan speed, and powder flow rate. The correlations between these parameters and the final properties of the samples were analysed, with a particular focus on microstructure, deposition defects and surface morphology.

Materials and Methods

The experimental campaign focused on the printing of $AlCoCr_2FeMo_{0.5}Ni$ High Entropy Alloy powder supplied by Heeger Materials Inc (CO, US). The powder had a particle size range of 45 – 106 μm, suitable for Directed Energy Deposition process. SS 316L austenitic stainless steel plate with a thickness of 10 mm was chosen as the substrate material. This choice aimed to minimize intergranular corrosion, prevent surface hardening – thanks to the low carbon content (< 0.03%) – and enhance oxidation resistance [6]. The chemical compositions of both the powder and substrate are reported in Table 1.

Table 1. Chemical compositions of the high-entropy alloy powder and substrate materials

[wt %]	***Al***	***Co***	***Fe***	***Cr***	***Mo***	***Ni***	***Mn***	***C***	***Si***	***N***
$AlCoCr_2FeMo_{0.5}Ni$	7.89	17.60	15.44	29.06	13.42	16.57	-	0.01	-	0.01
AISI 316L	-	-	bal.	18.58	0.44	8.40	1.69	0.02	0.44	0.11

The DED system used for the specimen production features a 6-axis ABB IRB 4600 robot, a GTV PS2/2 powder delivery system and a six-outlets GTV PN6625 nozzle with a standoff distance of 25 mm and a powder-jet focus of 2 mm. The heat source consists of a Laserline LDF-4500-60 diode laser with a maximum output power of 4.5 kW, equipped with OTS-5 focusing optics, resulting in a spot diameter of 2.2 mm on the print surface. Argon was used as both the carrier and shielding gas, with flow rates of 8 and 20 lpm, respectively. The experiment was organized into four progressively complex steps, with a decreasing number of samples per phase: (1) single-track depositions; (2) multi-track depositions with 8 adjacent tracks in a single-layer (2a) and double-layer (2b) configuration, and (3) multi-layer depositions with 8 layers using a scanning strategy that combines a contour path with a zig-zag infill pattern rotated by 90° at each layer. Single-track specimens were printed varying the main process parameters: laser power, scan speed, and powder flow rate. The laser source employed in the experimental campaign operates within a power range of 600 to 4500 W. To ensure comprehensive investigation, six power levels were selected to cover the entire range available, with a maximum limit of 3800 W imposed for safety considerations. Based on the chosen power values, the scanning speeds and powder feed rates were determined to achieve specific energy levels comparable to those reported in similar studies on AlCoCrFeNi alloys [3], [8], [9]. Table 3 summarizes the values considered in the study for each parameter. Specific energy (E) was calculated as:

$$E = \frac{P}{v \cdot D}$$

where P is the laser power, v is the scan speed, and D is the laser spot diameter.

Materials Research Proceedings 57 (2025) 99-106 https://doi.org/10.21741/9781644903735-12

Table 2. List of the experimental steps and deposition geometry

PHASE	DESCRIPTION	N. SPECIMENS	N. ADJACENT TRACKS	N. LAYERS
1	Single track	36	1	1
2A	Multi-track, 1 layer	12	8	1
2B	Multi-track, 2 layers	6	8	2
3	Multi-layer	2	25	8

Table 3. Laser power (P_L1 to P_L6), scan velocity (v_L1 to v_L3) and powder flow rate (g_L1 to g_L2) levels considered for single-track experiments

	L1	L2	L3	L4	L5	L6
POWER, *P* [W]	800	1400	2000	2600	3200	3800
SCAN VELOCITY, *V*	600	1020	1440			
POWDER FLOW RATE, *G*	10	17				

In order to determine the optimal process parameters for phases 2 and 3, a microstructural analysis of all the single tracks deposited in phase 1 was conducted by cutting cross-section from the center of the deposition, polishing and etching. The relative density was evaluated using a Zeiss AXIO Observer A1m optical microscope, while the microstructure was analyzed with a Tescan Mira3 SEM-FEG microscope. For the density evaluation, ImageJ software was used to calculate the porosity in the cross-section of each specimen. The relative density was then determined as (*100 – porosity*%), representing the percentage of the material's theoretical density achieved. Additionally, six 25 x 25 mm^2 single-layer specimens were fabricated to study the effects of laser power and scan speed on the deposition morphology, using the process parameters listed in the Results and Discussion section (Table 4). For each specimen, the surface profile of a 6.5 x 6.5 mm^2 area in the middle of the deposition was captured using a Keyence VHX-7000 digital optical microscope with 100x lens to generate 3D morphological maps. The surface maximum height (S_z) was calculated as the sum of the highest peak and the deepest valley within the area of interest, while the surface average roughness (S_a) represents the mean of the absolute height values at all points in the same area.

Results and Discussion

Process parameters optimization. In the single-track depositions, two criteria were established to define acceptable results: (i) absence of cracks or detachment and (ii) a relative density exceeding 99%. Visual inspection of the micrographs was used to verify the compliance with these requirements. The findings show that specimens fabricated with an energy density below 65 $J \cdot mm^{-2}$ are prone to cracking (Fig. 1). Among the crack-free depositions, samples produced at a scan speed of 600 $mm \cdot min^{-1}$ exhibited lower and more variable results compared to those produced at higher speeds. Tests conducted at 1020 and 1440 $mm \cdot min^{-1}$ achieved densities above 99.5%; consequently, the scan speed of 600 $mm \cdot min^{-1}$ was excluded from further testing. Summarizing the results of single-track experiments, requirements (a) and (b) were satisfied for scanning velocities v greater than 600 $mm \cdot min^{-1}$ and energy densities E greater than 65 $J \cdot mm^{-2}$. The final operating window was determined by solving this system of inequalities using the parameters listed in Table 3:

- For v = 1020 $mm \cdot min^{-1}$ it is required that P>2431 W. The power values that meet this condition are 2600, 3200 and 3800 W

Materials Research Proceedings 57 (2025) 99-106 https://doi.org/10.21741/9781644903735-12

- For v = 1440 mm·min^{-1} it is required that P>3432 W. Therefore, the only acceptable power value is 3800 W.

For both scanning speeds, the investigation in the following steps included also a power level slightly below the minimum acceptable threshold. This choice was based on the reasoning that a larger sample size, due to its longer interaction time, receives a higher total energy input, which could enable lower power levels to still achieve high densities.

Figure 1. Examples of single-track micrographs and their dependence on process parameters

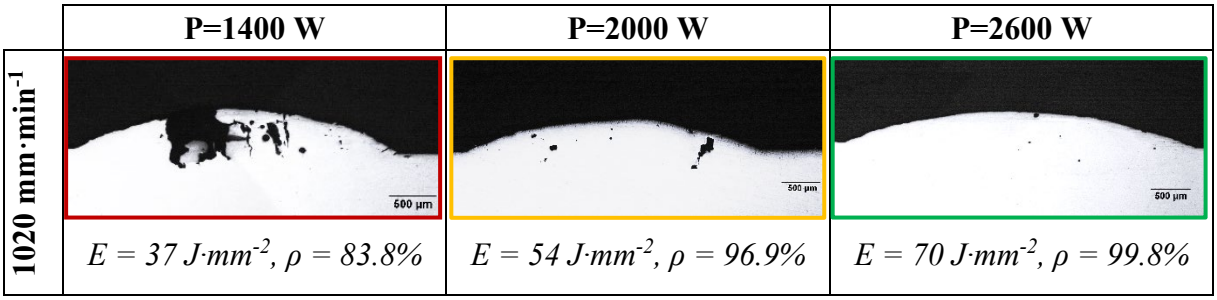

For multi-track tests in single-layer configuration (step 2a), the combinations of laser power and scan speed resulted from the previous analysis and summarized in Table 4 were deposited at both 10 and 17 g·min^{-1}.

Table 4. Combinations of process parameters used for multitrack tests

Specimen	***Power,*** *P [W]*	***Scan velocity,*** *v [mm·min^{-1}]*	***Specimen***	***Power,*** *P [W]*	***Scan velocity,*** *v [mm·min^{-1}]*
1	2000	1020	4	3800	1020
2	2600	1020	5	3200	1440
3	3200	1020	6	3800	1440

Cracks were observed in all tests conducted at 17 g·min^{-1}. Consequently, a powder flow rate of 10 g·min^{-1} was selected and all the combinations in Table 4 were tested with two overlapping layers. Conditions 2 and 6 produced depositions with low porosity and no cracks (Fig. 2a, 2b). As a result, these parameters combinations were used for eight-layers multi-track tests, which similarly achieved high quality depositions with densities greater than 99% (Fig. 2c,2d).

The presence of cracks may be associated with adhesion issues between the deposited material and the substrate. Although not observed in single-track tests, this defect could have been exacerbated by the repeated thermal cycles during multi-track tests. Furthermore, as shown in the phase diagram of the alloy under study (Fig. 2e), intermetallic compounds can form in addition to BCC phases. Specifically, the sigma phase is a hard and brittle intermetallic compound whose formation is facilitated by the presence of molybdenum [7]. The phase diagram indicates that the sigma phase occupies a broad region and forms over a wide temperature range, making it highly likely to form and contribute to crack formation within the material.

Materials Research Proceedings 57 (2025) 99-106 https://doi.org/10.21741/9781644903735-12

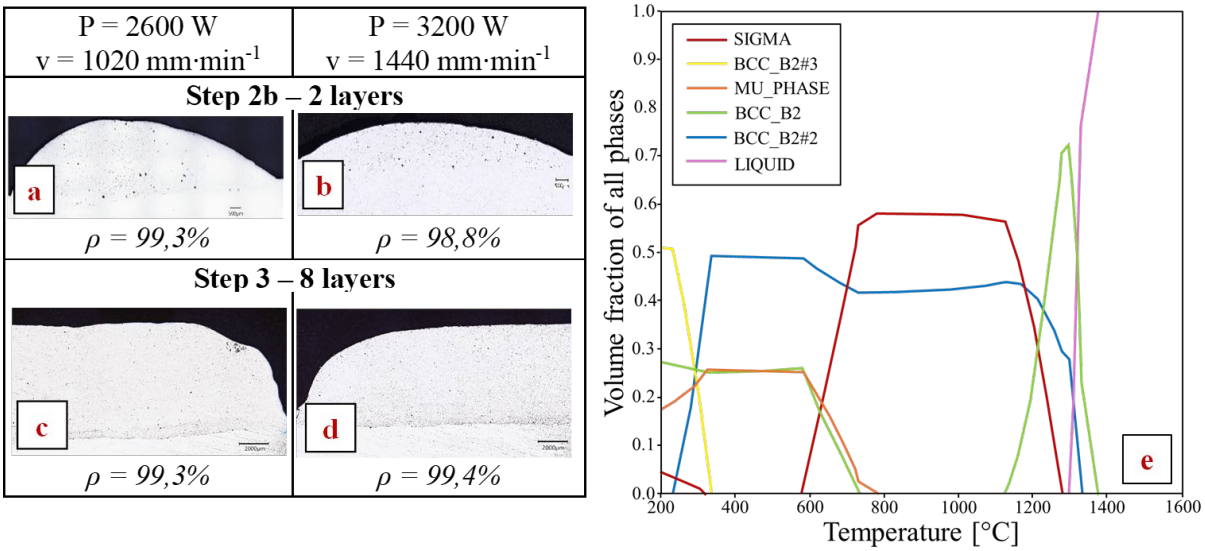

Figure 2. Photos of multitrack (a,b) and multilayer (c,d) tests with the optimal parameters; (e) phase diagram of $AlCoCr_2FeMo_{0.5}Ni$ alloy

Microstructural analysis. The microstructural study was performed comparing the results obtained both with optical and scanning electron microscopy, identifying four distinct regions within the deposition sections, consistent with observations by Sui et al. [3]: the interface, the planar grain zone, the transition zone, and the equiaxed grain zone.

The interface between the base material and the HEA deposition is characterized by a distinct change in microstructure. As shown in Fig. 3a, the lower section presents the austenitic grains of AISI 316L, while columnar HEA grains appear above the interface. Fig. 3b reveals a flake structure at the interface, with higher Fe and lower Al, Cr content, suggesting Fe diffusion from the substrate and possible segregation.

Above the dilution zone, elongated planar grains dominate the microstructure. Columnar grains grow in length when increasing the distance from the interface, influenced by the small grain size of the substrate and rapid cooling near the base. At higher deposition heights, slower cooling allows grain growth along the direction of heat flow, perpendicular to the interface. EDS results (Fig. 3c) show a higher concentration of Al and Fe within the crystals, while Cr and Mo tend to segregate at the grain boundaries. The presence of a Cr and Mo-rich phase is consistent with findings by Zhuang et al. [7].

Further from the interface, a transition from columnar to equiaxed grains occurs, visible under OM (Fig. 3d). The equiaxed grains nucleate in the liquid region ahead of the columnar grains, as described by Kurz et al. [10]. These differences in growth mechanisms result in varied morphologies: equiaxed grains form dendritic structures, while planar grains can exhibit cellular, planar, or dendritic patterns depending on local cooling conditions. A mixed microstructure is shown in Fig. 3e.

At greater deposition heights, grains fully transition to an equiaxed structure without a preferential orientation. At high-magnification, grain boundaries and fine dendritic structures are clearly distinguishable (Fig. 3f).

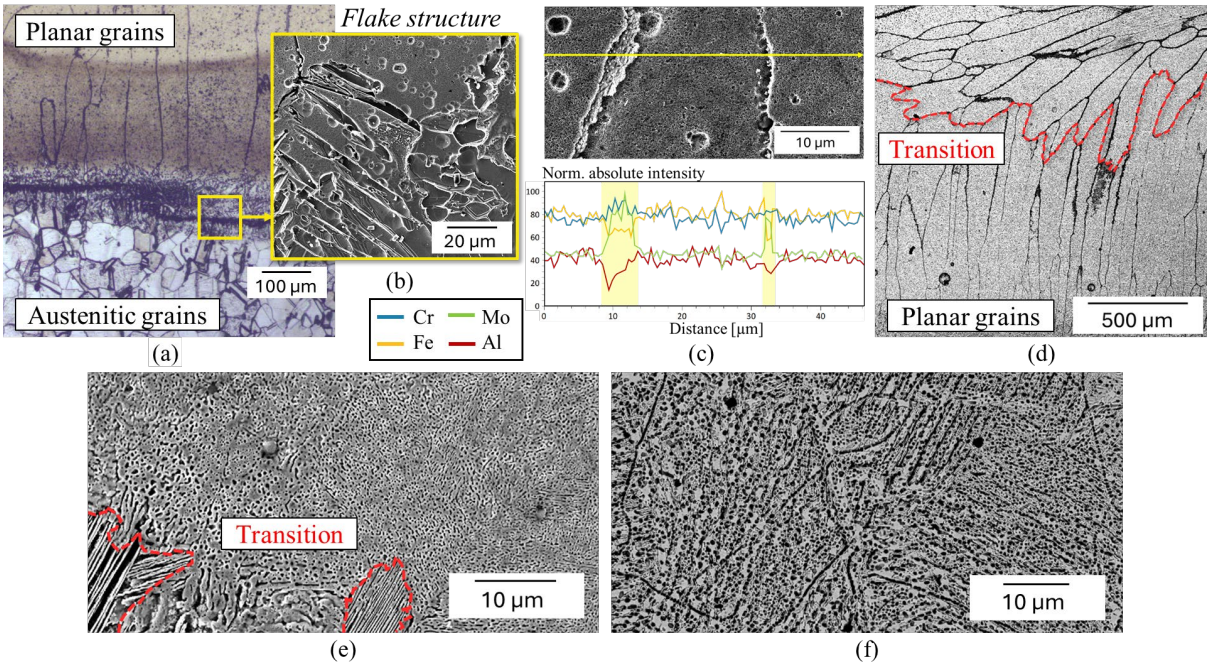

Figure 3. SEM and OM images of the interface (a,b), planar grain (c,d), transition (e,f) and equiaxed grain (g,h) zone

Morphological tests. Table 5 reports the average areal roughness (S_a and S_z) values for the morphological samples. Tests M1 and M3, conducted at a laser power of 800 W and scanning speeds of 600 and 1440 mm/min respectively, exhibited significantly higher roughness and spherical clusters on the surface (Fig. 4). This phenomenon occurs when material fails to solidify into continuous layers and, according to Liu et al. [11], it is linked to low energy input. In test M1, some of these clusters reached up to 1 mm in size, while in test M3, the surface particles were smaller and closer in size to the original powder. The formation of spherical clusters is attributed to the Plateau-Rayleigh instability: the molten pool elongates and fragments into islands at high scanning speeds to maintain uniform capillary pressure [12].

Table 5. Process parameters and average areal roughness values of morphological samples

#	P [W]	V [MM·MIN⁻	G [G·MIN^{-1}]	SA [µM]	Sz [µM]
M1	800	600	10	114	1013
M2	3800	600	10	33	302
M3	800	1440	10	45	467
M4	3800	1440	10	25	261
M5	2600	1020	10	20	283
M6	3200	1440	10	26	254

In contrast, tests M2 and M4, performed at 3800 W with the same scanning speeds (600 and 1440 mm·min^{-1} respectively), showed no spherical clusters but exhibited material accumulations (Fig. 4). This phenomenon, known as “humping”, is likely caused by hydrodynamic instability and occurs when the liquid material moves slower than the shielding gas. As stated by DebRoy et al. [12], humping appears to be more relevant at high scanning speeds and energy densities.

Finally, tests M5 and M6, produced using intermediate energy density values and the optimal process parameters, showed minimal spherical clusters and reduced humping defects. Test M5, conducted at 2600 W, had fewer humping defects compared to those performed at higher power

Materials Research Proceedings 57 (2025) 99-106 https://doi.org/10.21741/9781644903735-12

levels (3200 W and 3800 W). These results suggest that intermediate power and speed parameters effectively minimize morphological defects, leading to improved surface roughness. To achieve a more detailed analysis, the surface of the M5 sample underwent EDS examination to assess the distribution of alloying elements. The compositional map (Fig. 5) revealed a tendency to form two distinct types of clusters: one consisting solely of aluminum, which appears reflective in SEM images and is also visible to the naked eye, and another composed of the remaining alloying elements, which appears white and opaque. The differing behavior of aluminum compared to the other elements could be attributed to its lower melting point, potentially leading to localized vaporization in some areas.

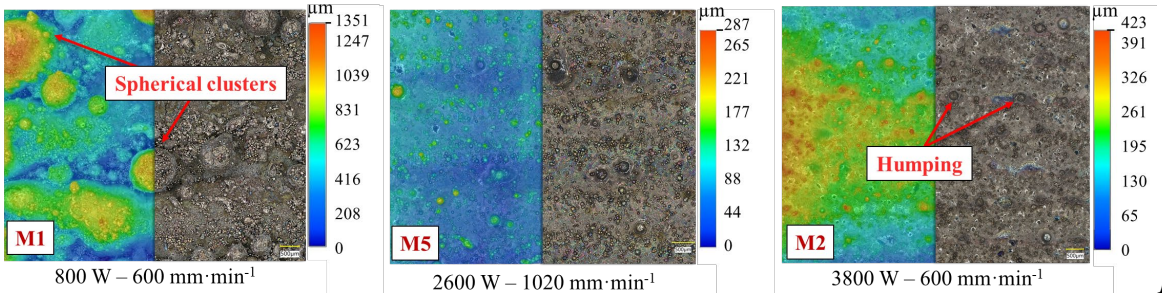

Figure 4. Examples of morphological maps for spherical clusters, humping and intermediate case

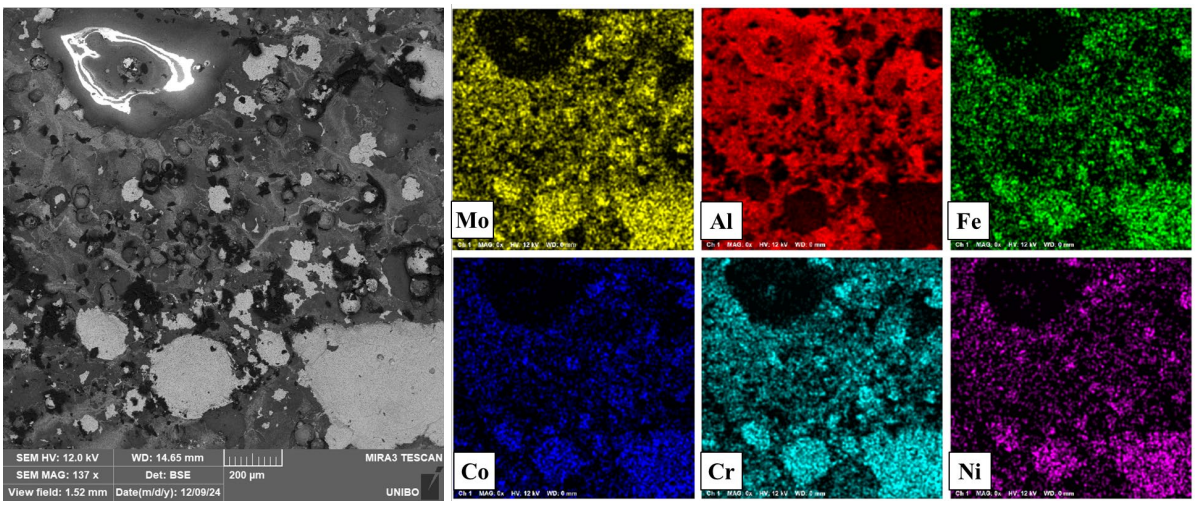

Figure 5. Compositional maps of the surface of M5 sample

Conclusions

This study demonstrated the feasibility of producing AlCoCr2FeMo0.5Ni high-entropy alloy coatings using Laser Directed Energy Deposition technology. The investigation of process parameters revealed that optimal combination of laser power, scanning speed, and powder flow rate are crucial for achieving high quality depositions with minimal defects and relative densities exceeding 99%. Specifically, intermediate energy density values minimized morphological issues such as spherical clusters and humping defects, leading to improved surface roughness.

The microstructural analysis identified four zones in the deposition with distinct microstructure, reflecting the influence of thermal and mechanical processing conditions. These findings highlight the potential of L-DED for tailoring HEA microstructures for aerospace applications. Future work should focus on further optimizing energy input to enhance the mechanical performance of HEA components.

References

[1] A. Morad e Y. Shash, «NICKEL BASE SUPERALLOYS USED FOR AERO ENGINE TURBINE BLADES», *The International Conference on Applied Mechanics and Mechanical Engineering*, vol. 16, fasc. 16, pp. 1–22, mag. 2014. https://doi.org/10.21608/amme.2014.35549

[2] M. Tokarewicz e M. Grądzka-Dahlke, «Review of Recent Research on AlCoCrFeNi High-Entropy Alloy», *Metals*, vol. 11, fasc. 8, Art. fasc. 8, ago. 2021. https://doi.org/sui

[3] Q. Sui *et al.*, «The microstructure and mechanical properties of the additive manufactured AlCoCrFeNi high entropy alloy», *Materials Science and Engineering: A*, vol. 833, p. 142507, gen. 2022. https://doi.org/10.1016/j.msea.2021.142507

[4] Z. Liang, Y. Zhang, Y. Liu, Z. Zhu, e H. Zhang, «Microstructure and properties of AlCoCrFeNi2.1 eutectic high-entropy alloy formed by laser melting deposition (LMD)», *Materials Letters*, vol. 317, p. 132092, giu. 2022. https://doi.org/10.1016/j.matlet.2022.132092

[5] S. Arun, N. Radhika, e B. Saleh, «Effect of Additional Alloying Elements on Microstructure and Properties of AlCoCrFeNi High Entropy Alloy System: A Comprehensive Review», *Met. Mater. Int.*, vol. 31, fasc. 2, pp. 285–324, feb. 2025. https://doi.org/10.1007/s12540-024-01752-3

[6] Q. Chao, T. Guo, T. Jarvis, X. Wu, P. Hodgson, e D. Fabijanic, «Direct laser deposition cladding of Al CoCrFeNi high entropy alloys on a high-temperature stainless steel», *Surface and Coatings Technology*, vol. 332, pp. 440–451, dic. 2017. https://doi.org/10.1016/j.surfcoat.2017.09.072

[7] Y. X. Zhuang, X. L. Zhang, e X. Y. Gu, «Effect of molybdenum on phases, microstructure and mechanical properties of Al0.5CoCrFeMo Ni high entropy alloys», *Journal of Alloys and Compounds*, vol. 743, pp. 514–522, apr. 2018. https://doi.org/10.1016/j.jallcom.2018.02.003

[8] Q. Sui *et al.*, «Strength-ductility balance of AlCoCrFeNi2.1 eutectic high-entropy alloy via additive manufacturing», *Journal of Materials Research and Technology*, vol. 30, pp. 1992–2003, mag. 2024. https://doi.org/10.1016/j.jmrt.2024.03.207

[9] J. An, Y. Zhou, M. Yan, Z. Liu, e Q. Zhu, «Effect of Heat Treatment on Microstructure and Mechanical Properties of Direct Energy Deposited AlCoCrFeNi2.1», *J Therm Spray Tech*, vol. 31, fasc. 5, pp. 1634–1648, giu. 2022. https://doi.org/10.1007/s11666-022-01390-4

[10] W. Kurz, C. Bezençon, e M. Gäumann, «Columnar to equiaxed transition in solidification processing», *Science and Technology of Advanced Materials*, vol. 2, fasc. 1, pp. 185–191, gen. 2001. https://doi.org/10.1016/S1468-6996(01)00047-X

[11] M. Liu, A. Kumar, S. Bukkapatnam, e M. Kuttolamadom, «A Review of the Anomalies in Directed Energy Deposition (DED) Processes & Potential Solutions - Part Quality & Defects», *Procedia Manufacturing*, vol. 53, pp. 507–518, 2021. https://doi.org/10.1016/j.promfg.2021.06.093

[12] T. DebRoy *et al.*, «Additive manufacturing of metallic components – Process, structure and properties», *Progress in Materials Science*, vol. 92, pp. 112–224, mar. 2018. https://doi.org/10.1016/j.pmatsci.2017.10.001